Cramér–Rao Bounds for Parametric Shape Estimation in Inverse Problems

Jong Chul Ye, *Member, IEEE*, Yoram Bresler, *Fellow, IEEE*, and Pierre Moulin, *Fellow, IEEE*

***Abstract*—We address the problem of computing fundamental performance bounds for estimation of object boundaries from noisy measurements in inverse problems, when the boundaries are parameterized by a finite number of unknown variables. Our model applies to multiple unknown objects, each with its own unknown gray level, or color, and boundary parameterization, on an arbitrary known background. While such fundamental bounds on the performance of shape estimation algorithms can in principle be derived from the Cramér–Rao lower bounds, very few results have been reported due to the difficulty of computing the derivatives of a functional with respect to shape deformation. In this paper, we provide a general formula for computing Cramér–Rao lower bounds in inverse problems where the observations are related to the object by a general linear transform, followed by a possibly nonlinear and noisy measurement system. As an illustration, we derive explicit formulas for computed tomography, Fourier imaging, and deconvolution problems. The bounds reveal that highly accurate parametric reconstructions are possible in these examples, using severely limited and noisy data.**

***Index Terms*—Cramér–Rao bounds, deconvolution, domain derivative, Fourier imaging, global confidence region, linear inverse problems, parametric shape estimation, performance analysis, Radon transform, tomography.**

I. Introduction

THE PROBLEM of estimating object boundaries from noisy measurements is encountered in applications such as computed tomography (CT), image deconvolution, synthetic aperture radar (SAR), and nonlinear inverse scattering. If the boundary is represented mathematically as a curve in $\mathbb{R}^2$, there is generally insufficient information to recover details of this boundary from limited measurements. This situation is typical of an ill-posed image reconstruction problem.

In such problems, the boundary is often parameterized by a finite number of unknown variables. Such a parametric formulation (for instance using B-splines [1] or Fourier descriptors [2], [3]) is a first step toward constructing a stable boundary estimation algorithm. This type of parameterization imposes smoothness on the reconstructed boundary and provides the basis for, e.g., an efficient maximum likelihood estimation algorithm. Once a suitable parametric model has been identified, fundamental bounds on the performance of shape estimation algorithms can in principle be derived by computing the Cramér–Rao lower bound (CRB).

Cramér–Rao lower bounds are widely used in problems where the exact minimum-mean-square error of an estimator is difficult to evaluate. The CRB provides an unbeatable performance limit for any unbiased estimator, and hence can be used to investigate the fundamental limits of parameter estimation problems, or as a baseline for assessing the performance of a specific estimator [4]. Furthermore, under fairly mild regularity conditions, the CRB is asymptotically achieved by the maximum likelihood estimator (MLE). Hence, the CRB can also serve as a predictor of the high-SNR or large sample performance of the MLE or other asymptotically efficient estimators. Finally, the CRB can be used for optimum design of the measurement system, e.g., by selecting sampling points to minimize a functional of the CRB matrix, such as its trace or determinant [5].

While CRB's are available for estimation of signal parameters such as target location [6]–[9], direction-of-arrival (DOA) [5], [10]–[12], and size and orientation of a scatterer [9], [13], [14], only recently has this type of analysis been conducted for estimation of target shapes [15], [16]. In the paper by Hero *et al.* [15], the boundary of a star-shaped object[1] is parameterized using B-splines, and CRB's for the B-spline coefficients are computed for several shapes in a magnetic resonance imaging problem. However, these results are applicable only to star-shaped objects.

For nonlinear inverse scattering problems, Ye, Bresler and Moulin [16] employed the domain derivative technique [17] to compute the CRB for arbitrarily shaped objects. The computation of the domain derivatives for nonlinear inverse problems is usually problem-dependent and does not admit a general formula. Hence it must be treated separately for each problem. The focus of the present paper is on linear inverse problems, for which explicit formulae can be given. Linear inverse problems provide a rich class of models, and underlie most (although not all) imaging problems of interest in science and engineering. Moreover, as we now emphasize, although the inverse problems we consider are classified as linear with respect to the object, they are *nonlinear* with respect to the boundary shape. Therein lies some of the difficulty of obtaining the CRB's for these problems. Furthermore, as will be explained on Section III-B, the

Manuscript received August 20, 2001; revised July 22, 2002. This work was supported by a grant from DARPA under Contract F49620-98-1-0498, administered by AFOSR, and by NSF Infrastructure under Grant CDA 96-24396. The associate editor coordinating the review of this manuscript and approving it for publication was Dr. Mark R. Luettgen.

J. C. Ye was the University of Illinois at Urbana-Champaign, Urbana, IL 61801 USA. He is now with Philips Research USA, Briarcliff Manor, NY 10510 USA (e-mail: jong.ye@philips.com).

Y. Bresler and P. Moulin are with the Coordinated Science Laboratory, Department of Electrical and Computer Engineering, University of Illinois at Urbana-Champaign, Urbana, IL 61801 USA (e-mail: ybresler@uiuc.edu).

Digital Object Identifier 10.1109/TIP.2002.806249

[1] A set $\mathcal{A} \in \mathbb{R}^n$ for $n \geq 2$ is called star-shaped if there exists a point $x \in \mathcal{A}$ such that any ray emanating from x crosses the boundary of $\mathcal{A}$ only once. In this case, the boundary $\partial\mathcal{A}$ can be parameterized by the angle with respect to x.

measurement processes we consider may introduce further nonlinearity, so that the dependence of measurements on the object itself is no longer linear. The techniques and results developed in this paper therefore have broad applicability in imaging problems.

The CRB's computed using the techniques of this paper can also be used to compute a global uncertainty region around the boundary [18], providing an easily interpreted geometric display of boundary uncertainty. A related idea has been applied to tomographic reconstruction by Hanson *et al.* [19]. The uncertainty regions in [19] were however constructed using Monte-Carlo simulations for a particular estimator. Hence, they are limited to that estimator, and are time-consuming to construct. In contrast, our global confidence region can be easily and quickly constructed using the CRB covariance matrix, even before the construction of an estimator is attempted.

This paper is organized as follows. Section II introduces the basic shape estimation problem. In Section III, we briefly review the statistical framework of parametric boundary estimation, and discuss the significance of the Cramér–Rao lower bound. Section IV introduces the domain derivative, which allows the computation of the CRB's in shape estimation problems. Section V derives the domain derivatives for CT, Fourier imaging, and deconvolution. The CRB is then computed for several illustrative examples in Section VI. Section VII extends our theory to an object composed of multiple domains. Conclusions are presented in Section VIII.

II. Shape Estimation Problem

Consider a real-valued image f consisting of a constant-valued 2-D object and a known background density $f_2(x, y)$:

$$f(x, y) = \begin{cases} f_1, & (x, y) \in D \\ f_2(x, y), & (x, y) \in \mathbb{R}^2 \backslash D. \end{cases} \tag{1}$$

The intensity f_1 and region D are unknown, whereas $f_2(x, y)$ is known for all $(x, y) \in \mathbb{R}^2$. This scenario models an object of constant but unknown intensity and unknown shape, partly occluding (or replacing) a *known* background. This situation arises in applications requiring the imaging of localized changes or anomalies in a reference object, or the imaging of objects on a homogeneous background. Particular imaging scenarios satisfying these assumptions will be discussed later in the context of specific imaging modalities. Small (and often unavoidable) unstructured deviations of the assumed background f_2 from its actual values will be accommodated by the uncertainties in the statistical measurement model (e.g., additive measurement noise) described in the sequel. The object is thus completely defined by its image value f_1 and its boundary $\Gamma = \partial D$. The support set D need not be a connected region, so the formulation includes the case of multiple objects.

Let $g = \mathcal{H}f$ be a general linear integral transformation of f, defined by

$$g(s, t) = \int_{-\infty}^{\infty} \int_{-\infty}^{\infty} f(x, y) h(x, y, s, t)\, dx\, dy, \qquad (s, t) \in \Omega \tag{2}$$

where $h: \mathbb{R}^2 \times \Omega \to \mathbb{R}$ is a known kernel, and Ω a subset of $\mathbb{R}^2$. We assume that f and h satisfy appropriate conditions so that g is well defined. For example, one such set of conditions is that f is bounded, and $h(\cdot, \cdot, s, t)$ is absolutely integrable for any $(s, t) \in \Omega$.

Suppose $g(s, t)$ is sampled at a finite number M of positions $\{s_m, t_m\}_{m=1}^M$. The estimation problem we consider is to estimate the object boundary Γ from noisy measurements $\{y_m\}_{m=1}^M$ of the samples $g_m = g(s_m, t_m)$, $m = 1, \ldots, M$. Our goal is to derive fundamental bounds on the estimation accuracy of Γ for specified statistics of the measurement noise. Examples of the linear operator (2) are as follows.

A. Computed Tomography

Consider tomographic reconstruction from line-integral projections or the samples of the 2-D Radon transform. The Radon transform g of a 2-D function f, is defined as the collection of line integrals of f along lines, indexed by these lines' angle s from the x-axis and at distance t from the origin:

$$g(s, t) = \int_{-\infty}^{\infty} \int_{-\infty}^{\infty} f(x, y) \delta(x \cos(s) + y \sin(s) - t)\, dx\, dy, \quad -\infty < t < \infty,\ 0 \le s < \pi, \tag{3}$$

where $\delta(\cdot)$ is the Dirac impulse. The function f is assumed to be such that (3) is well-defined [20]. For example, it is sufficient that the 2-D Fourier transform of f exist, which is satisfied if f is absolutely integrable. In turn, a sufficient condition for this in our setup, is that f_2 be bounded, sufficiently smooth, and supported on a bounded region, which is satisfied in all practical applications.

This reconstruction problem (and several variations thereof [20]) is of interest in numerous applications [21], of which medical x-ray CT is the best known. In medicine, the problem of shape estimation of constant density objects arises in the imaging of blood vessels or heart chambers filled with contrast agents, or in emission tomography of regions marked by radioactive tracers. It also arises in nondestructive evaluation of metal castings for the presence of cracks or bubbles, or monitoring nuclear reactor cores. In geophysics it may be an appropriate model for estimating the shape of an underground reservoir. The known background $f_2(x, y)$ in these applications may be obtained from baseline reference scans in medicine, CAD models in nondestructive evaluation, etc.

B. Fourier Imaging

The second problem we consider is Fourier imaging [22], [23]. This problem arises in applications such as synthetic aperture radar (SAR) [24], [25], diffraction tomography (DT) [6], magnetic resonance imaging (MRI) [26], and other image formation modalities [22]. In Fourier imaging, measurements are samples of the 2-D Fourier transform:

$$g(s,t) = \int_{-\infty}^{\infty} \int_{-\infty}^{\infty} f(x,y) e^{-j2\pi(sx+ty)}\, dx\, dy, \quad (s,t) \in \mathbb{R}^2. \tag{4}$$

The same sufficient conditions as in the computed tomography problem are applicable to the Fourier imaging problem too. We

note that the Fourier imaging formulation often arises as a linear approximation to inverse wave scattering problems [27]. Objects of interest in these applications are often essentially impenetrable (e.g., the conductive metal shell of an aircraft, or the surface of the earth in SAR) or fully penetrable (e.g., "sound soft" in the case of permittivity profile inversion [27]). In either case, the boundary conditions on the objects are such that the constant-valued object model is an accurate description. As in the tomography problem, the known background $f_2(x, y)$ in these applications may be obtained from baseline reference scans. For example, in the case of transient change detection (response to a stimulus in functional MRI, or the appearance of a target in SAR) an accurate image of the static background $f_2(x, y)$ may be easily obtained, because of the essentially unlimited time available for data acquisition. In other applications, such as imaging on a sky background, a constant background may be assumed.

C. Deconvolution

The last problem we consider is deconvolution—a ubiquitous problem in all areas of science and engineering. Suppose the image $f(x, y)$ of (1) is blurred with a shift-invariant point spread function $h(x, y)$. The noiseless blurred image $g(x, y)$ is given by

$$\begin{aligned} g(s, t) &= (h ** f)(s, t) \\ &= \int_{-\infty}^{\infty}\int_{-\infty}^{\infty} f(x, y)h(s-x, t-y)\,dx\,dy, \\ &\qquad (s, t) \in R_f \subset \mathbb{R}^2 \end{aligned} \tag{5}$$

where $**$ is the 2-D convolution, and R_f denotes the image domain, respectively. For the convolution $g(s, t)$ to be well defined, it is sufficient that one of f and h be bounded and the other absolutely integrable, which is satisfied in all practical applications. For instance, if the point spread function is Gaussian with width parameter ν, then (5) takes the form

$$\begin{aligned} g(s, t) = \int_{-\infty}^{\infty}\int_{-\infty}^{\infty} &\frac{1}{2\pi\nu^2} \\ &\cdot e^{-((s-x)^2+(t-y)^2/2\nu^2)} f(x, y)\,dx\,dy. \end{aligned} \tag{6}$$

Deconvolution is a key problem in imaging systems and seismic inversion [22]. As in the other imaging problems, the known background $f_2(x, y)$ in these applications may be obtained from baseline reference scans. For example, in the case of change detection in an optical surveillance problem, an accurate image of the static background $f_2(x, y)$ may be easily obtained from the previous scenes.

III. Statistical Framework for Parametric Shape Estimation

A. Parametric Boundary Model

Since the estimation of Γ from a finite number of noisy samples $\{y_m\}_{m=1}^M$ is generally an ill-posed inverse problem, a possible remedy is to represent the boundary Γ as a known function with a finite number of unknown parameters:

$$\Gamma = \{\boldsymbol{\zeta}(u; \boldsymbol{\phi}), u \in I\}, \tag{7}$$

where $\boldsymbol{\phi} = (\phi_1, \ldots, \phi_K) \in \mathbb{R}^K$ is an unknown parameter vector, and $I \subset \mathbb{R}$ an interval. Because object boundaries correspond to closed contours, I is a closed interval, and $\boldsymbol{\zeta}(u; \boldsymbol{\phi})$ a periodic function of u, with period equal to the length $|I|$. In particular, we use the series expansion model

$$\begin{aligned} \boldsymbol{\zeta}(u; \boldsymbol{\phi}) &= [\, x(u; \boldsymbol{\phi}), \quad y(u; \boldsymbol{\phi})\,]^T \\ &= \sum_{i=1}^{K} \phi_i \mathbf{b}_i(u), \qquad u \in I, \end{aligned} \tag{8}$$

where $\mathbf{b}_i(u) \in \mathbb{R}^2$ is the ith basis function. Parameterizations such as Fourier descriptors (FD) [2], [3], B-splines [1] and wavelet descriptors [28], [29] are special cases of this model and have been widely used for shape representation.[2]

Throughout the paper, we assume that the boundary Γ is a 1-manifold in $\mathbb{R}^2$, or of class C^1 in order to apply in Section IV standard results about the domain derivative, which require this condition.

In practice, this regularity condition is not too restrictive and implies that the boundary Γ is sufficiently smooth without any cusps and crossings. Equivalently, a parameterized-manifold $\boldsymbol{\zeta}(u)$, $u \in I$ should be continuously differentiable with respect to u, its inverse should be continuous to avoid any crossing, and $\dot{x}(u)^2 + \dot{y}(u)^2 \neq 0$ for all $u \in I$ to prevent any cusps, where $\dot{x}(u)$ and $\dot{y}(u)$ denote the derivatives of the x and y components of $\boldsymbol{\zeta}(u)$ with respect to u. These regularity conditions are in addition to the earlier condition that $\boldsymbol{\zeta}(u)$, $u \in I$ be periodic with period $|I|$.

Under the series expansion model (8), in order to satisfy these regularity conditions, the basis function $\mathbf{b}_i$: $I \to \mathbb{R}^2$, $i = 1, \ldots, K$ should be continuously differentiable. The conditions for avoiding intersecting boundaries and cusp are, however, more difficult to impose for each basis function $\mathbf{b}_i$, because these are global properties contributed by the linear combination of all basis functions. Therefore, we will assume that the parameters ϕ_i, $i = 1, \ldots, K$ are chosen such that the resultant boundary $\Gamma = \{\boldsymbol{\zeta}(u; \boldsymbol{\phi}), u \in I\}$ does not have crossings and cusps.

B. Cramér–Rao Inequality

The measurements $\mathbf{y} = \{y_m\}_{m=1}^M$ are a noisy version of $\mathbf{g} = \{g_m\}_{m=1}^M$. The measurement model is specified by a conditional probability density function (pdf) $p_{Y|\mathbf{g}}(\mathbf{y}|\mathbf{g})$, where $\mathbf{y}$ denotes a particular realization of the random vector Y. Note that this formulation includes the case where the observation involves a nonlinear transformation of $\mathbf{g}$ such as in x-ray or positron emission tomography problems where the measurement y_m is Poisson distributed with rate $\lambda_m = \lambda_T \exp(-g_m)$.

We denote the mth noise-free sample $g(s_m, t_m)$ by $g_m = g_m(\boldsymbol{\theta})$, where

$$\boldsymbol{\theta} = [\, \phi_1 \quad \cdots \quad \phi_K \quad f_1\,]^T \tag{9}$$

[2]The estimation of an "optimum" model order K can be done using model order selection criteria such as MDL [30], as illustrated in [31]. Because an unknown model order will increase the estimation error, the CRB's on the boundary shape still provide a lower bound on the pointwise error in estimation of the boundary even when K is unknown. The detailed analysis of the effects of unknown K is, however, outside the scope of this paper, and we will assume that the model order K is known *a priori*.

in order to show explicitly the dependence on the unknown parameter vector.[3] In view of the parametric representation (7) and (8) of the object, and the image formation model (2), $\mathbf{g}$ is completely determined by the unknown vector $\boldsymbol{\theta}$ and the known background f_2, and the statistics of Y can be described by

$$p_{Y|\mathbf{g}}(\mathbf{y}|\mathbf{g}) = p_{Y|\mathbf{g}(\boldsymbol{\theta})}(\mathbf{y}|\mathbf{g}(\boldsymbol{\theta})), \tag{10}$$

which we denote, for brevity, by $p(\mathbf{y}|\boldsymbol{\theta})$.

Given data $\mathbf{y}$ and its statistical description by $p(\mathbf{y}|\boldsymbol{\theta})$, the shape reconstruction problem has been reduced to a statistical parameter estimation problem. As is well-known, the variance of an unbiased estimator of $\boldsymbol{\theta}$ is subject to a fundamental limit—the Cramér–Rao lower bound (CRB). Moreover, under appropriate regularity conditions, the maximum likelihood estimator (MLE) achieves the CRB asymptotically [4]. Hence, the CRB is not only a lower bound, but is also useful for predicting the large sample or high SNR performance of the MLE, or other asymptotically efficient estimators. The accuracy of the shape estimate can in turn be assessed from the accuracy of the parameter estimate. In particular, one can then construct global confidence regions for the object boundary [18]. Here, we first concentrate on the derivation of a procedure for computing the CRB. According to the Cramér–Rao inequality, subject to some regularity conditions on the conditional pdf $p_{Y|\boldsymbol{\theta}}$, the $(K+1)\times(K+1)$ covariance matrix of the estimation error $\hat{\boldsymbol{\theta}} - \boldsymbol{\theta}$ for the unknown parameter $\boldsymbol{\theta}$ is bounded from below as [4]

$$\mathrm{Cov}\left(\hat{\boldsymbol{\theta}} - \boldsymbol{\theta}\right) \geq \mathbf{C}_{\boldsymbol{\theta}} \triangleq (\mathbb{I}_{\boldsymbol{\theta}})^{-1}, \tag{11}$$

for *any unbiased* estimate $\hat{\boldsymbol{\theta}}$ of $\boldsymbol{\theta}$. Here, the matrix inequality notation $A \geq B$ indicates that $A - B$ is positive semidefinite, with A and B being Hermitian positive semidefinite matrices. In (11), the Fisher information matrix, $\mathbb{I}_{\boldsymbol{\theta}}$, is the $(K+1)\times(K+1)$ matrix

$$\mathbb{I}_{\boldsymbol{\theta}} = E\left[\nabla_{\boldsymbol{\theta}} \ln p(\mathbf{y}|\boldsymbol{\theta}) \nabla_{\boldsymbol{\theta}}^T \ln p(\mathbf{y}|\boldsymbol{\theta})\right] \tag{12}$$

where $\ln p(\mathbf{y}|\boldsymbol{\theta})$ is the log-likelihood function, and $\nabla_{\boldsymbol{\theta}}$ denotes gradient with respect to θ.

C. Fisher Information Matrix

For any pdf $p(\mathbf{y}|\boldsymbol{\theta})$ for which the Fisher information matrix is well-defined, it follows from the chain rule that the entries of $\mathbb{I}_{\boldsymbol{\theta}}$ in (12) are (possibly nonlinear) functions of $g_m(\boldsymbol{\theta})$ and the derivatives $(\partial g_m(\boldsymbol{\theta}))/\partial\theta_i, i = 1, \ldots, K+1, m = 1, \ldots, M$.

For examples, if the noisy measurement Y_m is a Gaussian random variable with mean $g_m(\boldsymbol{\theta})$ and variance σ_m^2, under the additional assumption of independence of measurements at different locations, the (i, j)th element of the Fisher information matrix is given by

$$(\mathbb{I}_{\boldsymbol{\theta}})_{i,j} = \sum_{m=1}^{M} \frac{1}{\sigma_m^2} \frac{\partial g_m(\boldsymbol{\theta})}{\partial \theta_i} \frac{\partial g_m(\boldsymbol{\theta})}{\partial \theta_j}, \quad i, j = 1, \ldots, K+1, \tag{13}$$

[3]The measurement $g(s_m, t_m)$ is also a function of *known* background $f_2(x, y)$. However, this dependence is not explicitly expressed since $f_2(x, y)$ is assumed known.

whereas for the complex circular Gaussian noise with mean zero and variance $E|Y_m - g_m|^2 = 2\sigma_m^2$ we have

$$(\mathbb{I}_{\boldsymbol{\theta}})_{i,j} = \sum_{m=1}^{M} \frac{1}{\sigma_m^2} \mathrm{Re}\left[\left(\frac{\partial g_m(\boldsymbol{\theta})}{\partial \theta_i}\right)^* \frac{\partial g_m(\boldsymbol{\theta})}{\partial \theta_j}\right], \quad i, j = 1, \ldots, K+1, \tag{14}$$

where $\mathrm{Re}[\cdot]$ denotes the real part and the superscript $*$ denotes the conjugation.

While (13) and (14) appear simple, techniques for computing the derivatives $\{\partial g_m(\boldsymbol{\theta})/\partial\theta_i\}$ for models of the form (2) and (7), (8) have not been studied in the literature, except for special cases in a magnetic resonance imaging problem [9], [14], [15]. We now develop a general technique to compute those quantities in a generic linear inverse problem.

D. From CRB's to Global Confidence Regions

In practice, because $\boldsymbol{\zeta}(u; \boldsymbol{\theta})$ describes the geometry of an object, one is interested in assessing the quality of estimates of $\boldsymbol{\zeta}(u; \boldsymbol{\theta})$ in easily interpreted geometric terms. Rather than the quality of estimates of $\boldsymbol{\theta}$ itself, what is needed is a global quality measure for the entire boundary $\{\hat{\boldsymbol{\zeta}}(u; \boldsymbol{\theta}), \forall\, u \in I\}$. The CRB $\mathbf{C}_{\boldsymbol{\theta}}$ computed by the techniques of this paper can be used, as described in [18], to construct small-size *global confidence regions* in the asymptotic regime where the estimate is unbiased, efficient, and Gaussian. Bounds are given in [18] for the probability that the entire boundary estimate lies in the global confidence region. We illustrate the construction of such confidence regions in the numerical examples in Sections VI and VII.

IV. Domain Derivative

Combining the object model (1) and the noise-free measurement equation (2) yields

$$g(s, t) = f_1 \int_D h(x, y, s, t)\, dx\, dy + \int_{\mathbb{R}^2 \setminus D} f_2(x, y) \cdot h(x, y, s, t)\, dx\, dy, \quad (s, t) \in \Omega. \tag{15}$$

Equation (15) then defines a mapping J: $\{D\} \rightarrow \{g\}$ from the set of domains $\{D\}$, or equivalently, boundaries $\{\Gamma\}$, to the space of functions $\{g\}$. This mapping admits the general form:

$$g = J(D) = f_1 \int_D Z_1\, dS + \int_{\mathbb{R}^2 \setminus D} Z_2\, dS = c + \int_D Z dS, \tag{16}$$

where $dS = dx\, dy$, Z_1, Z_2, and $Z = f_1 Z_1 - Z_2$ are known functions on $\mathbb{R}^2$, D is the unknown object support, and $c = \int_{\mathbb{R}^2} Z_2\, dS$ is a function independent of D.

Given our parameterization of the boundary, we can rewrite (16) to display explicitly the dependence on $\boldsymbol{\theta}$,

$$g(\boldsymbol{\theta}) = J[D(\boldsymbol{\theta})] = c + \int_{D(\boldsymbol{\theta})} Z\, dS. \tag{17}$$

Our goal is compute the derivatives $\partial g(\boldsymbol{\theta})/\partial\theta_i$. The idea is to proceed using a two-step approach akin to the chain rule: i) find the change (deformation) of $D(\boldsymbol{\theta})$ produced by an infinitesimal change in θ_i; ii) then find the change in $\int_D Z\, dS$ produced by

the corresponding infinitesimal deformation of D. Because D is represented by its boundary $\Gamma(\boldsymbol{\theta})$ in our parameterization, it is more convenient to consider the corresponding deformations of $\Gamma(\boldsymbol{\theta})$.

The first step is easy. In view of (7)–(9), a change in θ_i to $\theta_i + t$ produces the deformed boundary

$$\Gamma_t = \Gamma + t\mathbf{b}_i = \{\mathbf{z} | \mathbf{z} = \boldsymbol{\zeta}(u) + t\mathbf{b}_i(u),\, u \in I\}, \tag{18}$$

where $\mathbf{b}_i$ is the ith basis function in the linear model (8) and $\boldsymbol{\zeta}(u)$ is the parametric representation of boundary given by (8).

The second step thus requires to compute the change in $\int_D Z\, dS$ produced by deformation of Γ to Γ_t for infinitesimal t. This is known as the *domain derivative* or the shape derivative, and has been studied extensively in structural mechanics [32]. Drawing upon these results we prove in Appendix A the following result:

Proposition 1: Let $D = D(\boldsymbol{\theta})$ be a domain with boundary Γ of class C^1. Suppose the boundary Γ is deformed as in (18). Then, the domain function (17) is shape differentiable with respect to boundary deformation $\mathbf{b}_i$, with domain derivative with respect to parameter θ_i:

$$\begin{aligned}\frac{\partial g}{\partial \theta_i} &= \delta J(D;\, \mathbf{b}_i) \\ &= \int_I Z(u)\big(\mathbf{b}_i^T \mathbf{n}\big)(u)\tau(u)\, du, \qquad i = 1, \ldots, K,\end{aligned} \tag{19}$$

where $Z(u) \triangleq Z[\boldsymbol{\zeta}(u)]$, $\tau(u) = \sqrt{\dot{x}(u)^2 + \dot{y}(u)^2}$ where $\dot{x}(u)$ and $\dot{y}(u)$ are the derivatives of the components of $\boldsymbol{\zeta}(u) = [x(u),\, y(u)]^T$, and $\mathbf{n}$ denotes the outer-normal vector of Γ.

The derivative with respect to $\theta_{K+1}(=f_1)$ is even simpler, of course, because it does not involve the domain derivative:

$$\frac{\partial g}{\partial \theta_{K+1}} = \frac{\partial g}{\partial f_1} = \int_D Z_1\, dS. \tag{20}$$

Using (19) [and (20) if f_1 needs to be estimated] we are ready to compute the CRB's for the examples mentioned earlier. We begin by deriving an explicit expression for $\partial g/\partial \theta_i$.

V. Domain Derivatives for Linear Inverse Problems

A. General Expressions

Combining (1) and (2) and separating the contribution of the domain D from the integral in (2), we obtain

$$\begin{aligned} g_m(\boldsymbol{\theta}) &= c(s_m,\, t_m) + \int_D Z(s_m,\, t_m,\, x,\, y)\, dx\, dy \\ &\triangleq J(D)(s_m,\, t_m), \qquad 1 \le m \le M, \end{aligned} \tag{21}$$

where

$$c(s_m, t_m) = \int_{\mathbb{R}^2} f_2(x,y) h(x,y,s_m,t_m)\, dx\, dy \tag{22}$$

$$Z(s_m, t_m, x, y) = (f_1 - f_2(x,y)) h(x,y,s_m,t_m). \tag{23}$$

Using (19), (21), and (23), we have

$$\frac{\partial g_m(\boldsymbol{\theta})}{\partial \theta_i} = \int_I \Delta f(u) h[x(u), y(u), s_m, t_m] \mathbf{b}_i^T(u) \mathbf{n}(u) \tau(u)\, du, \tag{24}$$

$$\Delta f(u) \triangleq f_1 - f_2[x(u), y(u)], \tag{25}$$

where

$$\tau(u) = \sqrt{\dot{x}(u)^2 + \dot{y}(u)^2} = \left\| \sum_{i=1}^M \theta_i \dot{\mathbf{b}}_i(u) \right\|, \tag{26}$$

$\dot{\mathbf{b}}_i(u)$ denotes the derivative of $\mathbf{b}_i$ with respect to u, and $\|\cdot\|$ denotes the Euclidean norm. In (24), the outer-normal vector $\mathbf{n}$ at $(x(u),\, y(u))$ is given by

$$\mathbf{n}(u) = \frac{1}{\tau(u)} \begin{bmatrix} \dot{y}(u) \\ -\dot{x}(u) \end{bmatrix} = \frac{\sum_{i=1}^M \theta_i \left[\dot{b}_i^y(u),\, -\dot{b}_i^x(u)\right]^T}{\left\| \sum_{i=1}^M \theta_i \dot{\mathbf{b}}_i(u) \right\|} \tag{27}$$

and so

$$\mathbf{b}_i^T \mathbf{n} = \frac{\sum_{j=1}^M \theta_j \left(b_i^x \dot{b}_i^y - b_i^y \dot{b}_i^x \right)}{\left\| \sum_{i=1}^M \theta_i \dot{\mathbf{b}}_i \right\|}, \tag{28}$$

where b_i^x and b_i^y denote the x and y components of $\mathbf{b}_i$, respectively. The derivative with respect to $\theta_{K+1}(=f_1)$ is given by

$$\frac{\partial g_m(\boldsymbol{\theta})}{\partial \theta_{K+1}} = \frac{\partial g_m(\boldsymbol{\theta})}{\partial f_1} = \int_D h(x,\, y,\, s_m,\, t_m)\, dx\, dy. \tag{29}$$

An important though somewhat expected observation that follows from (24), is the following. Although the measurements y_m, and in fact the existence of the transforms that define them, often depend on all of the background f_2, the Fisher information matrix only depends on the values of the background f_2 on the boundary Γ of the domain D.

B. Computed Tomography

Combining (2), (3), and (24) it follows that

$$\frac{\partial g_m(\boldsymbol{\theta})}{\partial \theta_i} = \int_I \delta(F_m(u)) G(u)\, du \tag{30}$$

where $\delta(\cdot)$ denotes the Dirac impulse and

$$F_m(u) = x(u)\cos(s_m) + y(u)\sin(s_m) - t_m \tag{31}$$

$$G(u) = \Delta f(u) \mathbf{b}_i^T(u) \mathbf{n}(u) \tau(u). \tag{32}$$

Note that in (30) if the equation $F_m(u) = 0$ has no solution on I, the integral is trivially zero. However, when $F_m(u) = 0$ does have a solution, multiple such solutions may exist, all contributing to the integral. Lemma 1 provides the formula for the integral accounting for all these contributions.

Lemma 1: Let functions F: $I \to \mathbb{R}$ be continuously differentiable and G: $I \to \mathbb{R}$ be continuous, where $I \subseteq \mathbb{R}$. Suppose furthermore $F(u)$ has L isolated roots $u_l \in I$, $l = 1, \ldots, L$

such that $F(u_l) = 0$ and $F'(u_l) \neq 0$. Then, if F does not have roots on boundary points of I, or if I is a closed interval and F periodic on I with period equal to its length $|I|$, we have

$$\int_I \delta(F(u))G(u)\,du = \sum_{l=1}^{L} \frac{G(u_l)}{|F'(u_l)|}, \tag{33}$$

where $\delta(\cdot)$ is the Dirac delta function, F' denotes the derivative of F, and $|\cdot|$ is the absolute value.

Proof: See Appendix B. □

Note that if any of the roots of $F(u)$ is multiple, then $F'(u_1) = 0$ and (33) is not defined. An example of this case will be presented in Section VI-A, demonstrating that in our application of the lemma this case corresponds to violation of the regularity conditions of the CRB.

Now we apply Lemma 1 to (30). Let $L(m)$ denote the number of solutions of $F_m(u) = 0$, and $u_l^m \in I$ denote the lth such solution, i.e., [by (31)]

$$x(u_l^m; \boldsymbol{\theta})\cos(s_m) + y(u_l^m; \boldsymbol{\theta})\sin(s_m) - t_m = 0. \tag{34}$$

Referring to Fig. 1, we identify $u_l^m \in I$ as the lth intersection of the boundary Γ with the line indexed by (s_m, t_m). Using Lemma 1 and (34), we have

$$\frac{\partial g_m(\boldsymbol{\theta})}{\partial \theta_i} = \sum_{l=1}^{L(m)} \frac{\Delta f(u_l^m)\mathbf{b}_i(u_l^m)^T\mathbf{n}(u_l^m)\tau(u_l^m)}{|\cos(s_m)\dot{x}(u_l^m) + \sin(s_m)\dot{y}(u_l^m)|}, \quad i = 1, \ldots, K, \tag{35}$$

where

$$\Delta f(u_l^m) = f_1 - f_2(x(u_l^m), y(u_l^m)). \tag{36}$$

By (29), the derivative with respect to f_1 is given by

$$\frac{\partial g_m(\boldsymbol{\theta})}{\partial \theta_{K+1}} = \frac{\partial g_m(\boldsymbol{\theta})}{\partial f_1} = \int_D \delta(x\cos(s_m) + y\sin(s_m) - t_m)\,dx\,dy, \tag{37}$$

which is a line integral projection of the indicator function of the domain D. Referring again to Fig. 1, this quantity equals the sum of the lengths of the chords formed by the intersection of the line parameterized by (s_m, t_m) with the domain D. The lengths can be computed by solving the appropriate equations (34) to find the intersection of the line parameterized by (s_m, t_m) with the parameterized boundary. The Fisher information matrix is then obtained by substituting (35) and (37) into (13).

C. Fourier Imaging

In this case,

$$h(x, y, s, t) = \exp\{-j2\pi(sx + ty)\}. \tag{38}$$

Therefore, we have

$$\frac{\partial g_m(\boldsymbol{\theta})}{\partial \theta_i} = \int_I \Delta f(u) e^{-j2\pi[s_m x(u) + t_m y(u)]}\left(\mathbf{b}_i^T\mathbf{n}\right)(u)\tau(u)\,du, \tag{39}$$

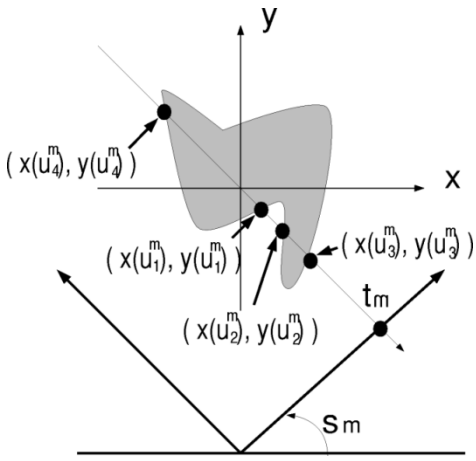

Fig. 1. Set of $\{(x(u_l^m),\ y(u_l^m))\}_{l=1}^{L(m)}$ of line-boundary intersections for a tomography problem.

where $\Delta f(u) = f_1 - f_2[x(u),\ y(u)]$ and τ and $\mathbf{b}_i^T\mathbf{n}$ are given by (26) and (28), respectively. By (29), the derivative with respect to f_1 is given by

$$\frac{\partial g_m(\boldsymbol{\theta})}{\partial \theta_{K+1}} = \frac{\partial g_m(\boldsymbol{\theta})}{\partial f_1} = \int_D e^{-j2\pi(s_m x + t_m y)}\,dx\,dy, \tag{40}$$

which is the Fourier transform of the indicator function of D, evaluated at $(t_m,\ s_m)$.

The following alternative expression, involving a 1-D instead of a an area integral, is obtained using Green's theorem [33]:

$$\begin{aligned}\int_D & e^{-j2\pi(s_m x + t_m y)}dx\,dy \\ &= \tfrac{1}{2}\int_I \left(\int_0^{x(u)} e^{-j2\pi(s_m z + t_m y(u))}\,dz\right)\dot{x}(u)\tau(u)\,du \\ &\quad - \tfrac{1}{2}\int_I \left(\int_0^{y(u)} e^{-j2\pi(s_m x(u) + t_m z)}\,dz\right)\dot{y}(u)\tau(u)\,du.\end{aligned} \tag{41}$$

This expression is particularly convenient when the boundary is parameterized by (8). Even when it can not be evaluated in closed form, its numerical evaluation requires, in general, less computation for given accuracy than that for the area integral in (40).

D. Deconvolution

The formulae are essentially the same as the general formulae (24) and (29), hence omitted here.

VI. CRB for Connected Boundaries

In this section, we compute Cramér–Rao bounds for boundary estimation of a single domain in several imaging examples, using the results of Section V.

A. Estimation of Radius of a Circle on a Flat Background

To illustrate the mechanics of computing the bounds, and verify that the results conform with intuition, we consider in this subsection a particularly simple example. Because our focus is on the domain derivative technique, which is not involved in

computing the derivative with respect to f_1 in (20), we assume in the examples that f_1 is known. The results for unknown f_1 can be obtained using (37), (40), or (29) in the respective examples, and would show increased error bounds on the unknown shape parameters, because of the additional uncertainty.

We provide a closed-form expression of the Cramér–Rao bounds for estimating the radius of a disk with known density f_1 on a flat background with

$$f_2(x, y) = \begin{cases} f_2: & (x, y) \in \Lambda \\ 0: & \text{else,} \end{cases}$$

where the support of the background Λ is a region that encompasses the unknown domain, i.e., $D \subset \Lambda$. As discussed earlier, the bounds only depend on the values of $f_2(x, y)$ at the boundary Γ, so the particular shape and size of Λ do not matter. However, to ensure that the different transforms we consider are all well-defined, we assume that Λ is a known bounded region.

For a circular domain D centered at origin, the boundary $\Gamma = \partial D$ is given by

$$\Gamma = \left\{ r \begin{bmatrix} \cos(u) \\ \sin(u) \end{bmatrix} ;\ u \in [0,\, 2\pi) \right\}, \tag{42}$$

where $r > 0$ is the unknown radius to be estimated (hence $\boldsymbol{\theta} = r$). In this case, for all $u \in [0,\, 2\pi)$ we have

$$\mathbf{b}_1(u) = \begin{bmatrix} \cos(u) \\ \sin(u) \end{bmatrix}, \quad \mathbf{n}(u) = \begin{bmatrix} \cos(u) \\ \sin(u) \end{bmatrix},$$
$$\tau(u) = r, \quad \mathbf{b}_1^T \mathbf{n} = 1. \tag{43}$$

Now we derive the CRB in closed form for estimation of r from noisy measurements in problems of computed tomography, Fourier imaging, and deconvolution. For simplicity, we assume that we have a single noisy measurement at $(s_1,\, t_1)$.

Computed Tomography: Assume the real Gaussian model so that the Fisher information matrix is given by (13). In order to apply (35), we first need to solve the trigonometric equation (34):

$$x(u)\cos(s_1) + y(u)\sin(s_1) - t_1 = 0. \tag{44}$$

Since $x(u) = r\cos(u)$ and $y(u) = r\sin(u)$, we obtain

$$t_1 = r\cos(u)\cos(s_1) + r\sin(u)\sin(s_1) = r\cos(u - s_1). \tag{45}$$

Equation (45) has zero, one, or two solutions $u_1,\, u_2 \in [0,\, 2\pi)$ depending on the value of t_1 relative to r. Using (11), (13), (35) and (43), we derive

$$\mathbf{C}_r = \mathbb{I}^{-1} = \begin{cases} \dfrac{\sigma_1^2(1 - t_1^2/r^2)}{4(f_1 - f_2)^2}, & |t_1| < r \\ \infty, & |t_1| > r \\ \text{undefined}, & t_1 = r \end{cases} \tag{46}$$

Equation (46) reveals that the error bound is proportional to the noise variance and to the inverse of the square of the object-to-background contrast (if $|t_1| < r$). The bound is independent of the view angle s_1, which is to be expected, because of the circular symmetry in the problem. Furthermore, if the ray does not intersect the disk D, the measurement does not convey any information about the domain D, and the error bound is infinite. These results are quite intuitive. What requires some interpretation, is the behavior of the bound near $t_1 = r$. First, at $t_1 = r$, we have $\cos(s_m)\dot{x}(u_l^m) + \sin(s_m)\dot{y}(u_l^m) = 0$ in (35), so that the derivative $\partial g_m(r)/\partial r$ is not defined, and the regularity conditions for the CRB are not satisfied. This is an instance of the case mentioned below Lemma 1, where $F'(u_1) = 0$. Next, for $|t_1|$ smaller than r but sufficiently close to it, $\partial g_m(r)/\partial r$ can be arbitrarily large—because of the steepness of the circle function at that point. So the CRB vanishes as $|t_1| \uparrow r$.

Fourier Imaging: We assume the complex Gaussian model so that the Fisher information matrix is given by (14). Using (11), (14), (39), and (43), we obtain

$$\begin{aligned} \mathbf{C}_r &= \frac{\sigma_1^2}{r^2(f_1 - f_2)^2} \left| \int_0^{2\pi} e^{-j2\pi(s_1 r\cos(u) + t_1 r\sin(u))}\, du \right|^{-2} \\ &= \frac{\sigma_1^2}{r^2(f_1 - f_2)^2} \left| \int_0^{2\pi} \exp\{-j2\pi r\omega_1\cos(u)\}\, du \right|^{-2} \\ &= \frac{\sigma_1^2}{4\pi^2 r^2(f_1 - f_2)^2} \left| J_0(2\pi r\omega_1) \right|^{-2}, \end{aligned} \tag{47}$$

where the radial frequency ω_1 is given by $\omega_1 = \sqrt{s_1^2 + t_1^2}$ and $J_0(\cdot)$ denotes the zeroth order Bessel function:

$$J_0(x) = \frac{1}{2\pi} \int_0^{2\pi} \exp(jx\cos(u))\, du. \tag{48}$$

As shown in (47), the bound $\mathbf{C}_r$ is a function of the radial frequency ω_1 of the sampling point $(s_1,\, t_1)$ in the Fourier domain. $\mathbf{C}_r$ is lower bounded by

$$\mathbf{C}_r \geq \frac{\sigma_1^2}{4\pi^2 r^2(f_1 - f_2)^2}, \tag{49}$$

because $|J_0(x)| \leq 1$ for all x, with equality at $x = 0$. The lower bound in (49) is achievable if and only if the sampling point is at the origin, i.e., $(s_1,\, t_1) = (0,\, 0)$. This is quite an intuitive result, which indicates that of all Fourier samples, the DC coefficient conveys the most information about the size of the circular domain D. Hence the CRB is smallest with a DC measurement.

Deconvolution: Assume the real Gaussian model so that the Fisher information matrix is given by (13). Using (11), (13), and (43), for the Gaussian blur model (6) we have

$$\begin{aligned} \mathbf{C}_r &= \frac{4\pi^2\nu^4\sigma_1^2}{r^2(f_1 - f_2)^2} \\ &\quad \cdot \left[\int_0^{2\pi} e^{-((s_1 - r\cos(u))^2 + (t_1 - r\sin(u))^2/2\nu^2)}\, du \right]^{-2} \\ &= \frac{\sigma_1^2}{(f_1 - f_2)^2} \frac{\nu^4}{r^2} \exp\left(\frac{r^2 + d^2}{\nu^2} \right) \left[I_0\left(\frac{rd}{\nu^2} \right) \right]^{-2}, \end{aligned} \tag{50}$$

where $d = \sqrt{s_1^2 + t_1^2}$ and $I_0(x)$ denotes the modified Bessel function of order zero:

$$I_0(x) = \frac{1}{2\pi} \int_0^{2\pi} \exp(x\cos(u))\, du. \tag{51}$$

Equation (50) shows that $\mathbf{C}_r$ is again a function of the distance d of sampling point (s_1, t_1) from the origin. For any fixed radius r of the disk, there is a distance d for the sampling point, which minimizes the bound. For example, for $r = 5$ and $\nu = 2$, the minimizing distance for the sampling point is $d_{\min} \simeq 4.5$. Likewise, for any fixed sampling point there is an optimum radius r of circular domain that minimizes $\mathbf{C}_r$. For example, if $(s_1, t_1) = (0, 0)$, then $d = 0$, and (50) can be further simplified as

$$\mathbf{C}_r = \frac{\sigma_1^2}{(f_1 - f_2)^2} \frac{\nu^4}{r^2} \exp\left(\frac{r^2}{\nu^2}\right). \tag{52}$$

A simple calculation shows that $\mathbf{C}_r$ of (52) is minimized if the domain D has radius $r = \nu$.

B. Estimation of Tumor on MRI Scan of Human Brain

We now turn to a more realistic imaging problem motivated by image reconstruction from sparse Fourier samples [34]–[37]. Consider the 128×128 MRI scan of a human brain with a tumor in Fig. 2(a). The image has 256 gray levels and was taken from a Harvard University medical database [38]. We parameterize the boundary of the tumor using Fourier descriptors (FD) [2], [3]:

$$\begin{aligned} x(u) &= a_0 + \sum_{i=1}^{L} (a_i \cos(iu) + a_{L+i} \sin(iu)) \\ y(u) &= b_0 + \sum_{i=1}^{L} (b_i \cos(iu) + b_{L+i} \sin(iu)), \end{aligned} \tag{53}$$

where $L = 15$. In order to overcome the ambiguity due to the starting point of the contour, in (53) the constraint $a_{L+1} = b_1$ is imposed [16]. Hence, the resulting parameter vector $\boldsymbol{\theta}$ is:

$$\boldsymbol{\theta} = [\, a_0 \quad a_1 \quad \cdots \quad a_{2L} \quad b_0 \quad b_2 \quad \cdots \quad b_{2L} \,]^T \in \mathbb{R}^{4L+1}. \tag{54}$$

The tumor is assumed to have constant intensity.

Suppose that 64 uniformly spaced Fourier samples are taken. This corresponds to $64/(128^2) = 0.4\%$ of the Nyquist sampling rate that would be required to avoid spatial aliasing for this 128×128 image. Suppose furthermore we have a full reference MRI scan of the healthy brain, and know *a priori* the intensity of the tumor, and the number of FD coefficients. Then, the imaging problem can be formulated as shape estimation of the tumor on the known background. Note that in this simulation the known background image has *inhomogeneous* density, and the boundary of the tumor is *not* star-shaped. Using the techniques described in Section V, we calculated the CRB for the unknown FD coefficients.

The CRB matrix $\mathbf{C}_{\boldsymbol{\theta}}$ is 61×61, and even its 61-element diagonal is unwieldy, and hard to interpret. Instead we have applied the global confidence region technique of [18] to the example of Fig. 2(a) and used the computed $\mathbf{C}_{\boldsymbol{\theta}}$ to compute, in turn, the 98% asymptotic global confidence region, which is readily visualized. Consider an example where the Fourier samples are corrupted with additive complex Gaussian noise with a standard deviation σ equal to 20% of the rms value of the noise-free measurements. (We denote the corresponding signal-to-noise-ratio by SNR = 5.) Fig. 2(b) illustrates the resulting asymptotic global confidence region, in which asymptotically any unbiased estimate of the boundary will lie with 98% probability. This bound suggests that accurate estimates are possible even at low sampling rates, if we have a parametric description of the tumor shape and know both the density of the tumor and the MRI scan of the healthy brain.

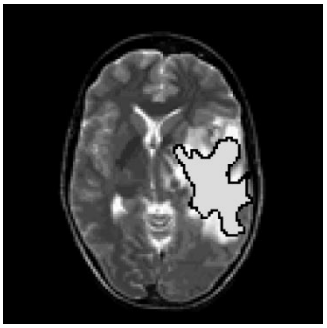

(a)

(b)

Fig. 2. (a) MRI scan of a human brain with tumor and (b) 98% global confidence region (indicated by the black region) for the boundary estimate using Fourier data corrupted by complex Gaussian additive noise at SNR = 5.

VII. Partitioned Density With Multiple Boundaries

A. Partitioned Density

This section extends our previous results to more general image configurations than (1), which assumes f is constant over D. Suppose the image can be partitioned into two disjoint regions,

$$f(x, y) = \begin{cases} f_1(x, y), & (x, y) \in D \\ f_2(x, y), & (x, y) \in \mathbb{R}^2 \backslash D, \end{cases} \tag{55}$$

where the background image $f_2(x, y)$ is known, and the unknown domain D is a union of sub-domains D_j, $j = 1, \ldots, L$:

$$D = \bigcup_{j=1}^{L} D_j. \tag{56}$$

Each boundary $\Gamma_j = \partial D_j$ is parameterized as

$$\Gamma_j = \{\boldsymbol{\zeta}_j(u; \boldsymbol{\theta}_j) : u \in I = [0, 2\pi)\}, \tag{57}$$

where $\boldsymbol{\theta}_j \in \mathbb{R}^{K_j}$ denotes a separate unknown parameter vector. Thus, the entire domain D is parameterized by the parameter vector $\boldsymbol{\theta} = [\boldsymbol{\theta}_1^T, \ldots, \boldsymbol{\theta}_K^T]^T$ of dimension $K = \sum_{j=1}^{L} K_j$. In general, the sub-domains D_j need not be disjoint, hence the domain D can be further partitioned into P disjoint regions:

$$D = \bigcup_{k=1}^{P} \Omega_k, \qquad \Omega_j \cap \Omega_k = \varnothing, \, j \neq k. \tag{58}$$

Furthermore, for each sub-domain D_j, there exists an index set $Q(j) \subset \{1, \ldots, P\}$ such that

$$D_j = \bigcup_{k \in Q(j)} \Omega_k. \tag{59}$$

We require $f_1(x, y)$ to be constant over each set Ω_k:

$$f_1(x, y) = \sum_{k=1}^{P} f_1^k \chi_{\Omega_k}(x, y) \tag{60}$$

where χ_{Ω_k} denotes the indicator function of the set Ω_k, and f_1^k is a constant. The partitioned density model (60) is quite general and can also serve an approximation to continuous densities.

B. Computation of the CRB

Hero *et al.* [15] conjectured that to derive performance bounds for the case of multiple domains, detection theoretical analysis using hypothesis testing would be necessary. This problem can however be addressed in an estimation framework.[4] Combining the object model (55) and the measurement equation (2), we can represent $g(x, y)$ with respect to each domain D_j:

$$\begin{aligned} g(s, t) = &\int_{D_j} f_1(x, y) h(x, y, s, t)\, dx\, dy \\ &+ \int_{\mathbb{R}^2 \setminus D} f_2(x, y) h(x, y, s, t)\, dx\, dy \\ &+ \int_{D \setminus D_j} f_1(x, y) h(x, y, s, t)\, dx\, dy. \end{aligned} \tag{61}$$

From the partitioned density in (60), we define:

$$f_{1,j}(x, y) = \sum_{k \in Q(j)} f_1^k \chi_{\Omega_k}(x, y) \tag{62}$$

$$f_{1,j^c}(x, y) = \sum_{k \in \{1, \ldots, P\} \setminus Q(j)} f_1^k \chi_{\Omega_k}(x, y). \tag{63}$$

Using (61)–(63), we then have

$$\frac{\partial g(\boldsymbol{\theta})}{\partial \theta_i^{(j)}} = \delta J\left(D, \mathbf{b}_i^{(j)}\right) = \int_{\Gamma_j} Z_j \left\langle \mathbf{b}_i^{(j)}, \mathbf{n} \right\rangle d\Gamma, \tag{64}$$

where $\theta_i^{(j)}$ and $\mathbf{b}_i^{(j)}$ denote the ith element of $\boldsymbol{\theta}_j$ and the corresponding basis function, respectively, and

$$Z_j(x, y, s, t) = (f_{1,j}(x, y) - f_{1,j^c}(x, y)) h(x, y, s, t). \tag{65}$$

Furthermore, the derivative with respect to the pixel value f_1^k is given by

$$\frac{\partial g(\boldsymbol{\theta})}{\partial f_1^k}(s, t) = \int_{\Omega_k} h(x, y, s, t)\, dS. \tag{66}$$

[4]However, the comments in Footnote 2 also apply to the estimation of the number L of subdomains, or regions P, if these are unknown *a priori*.

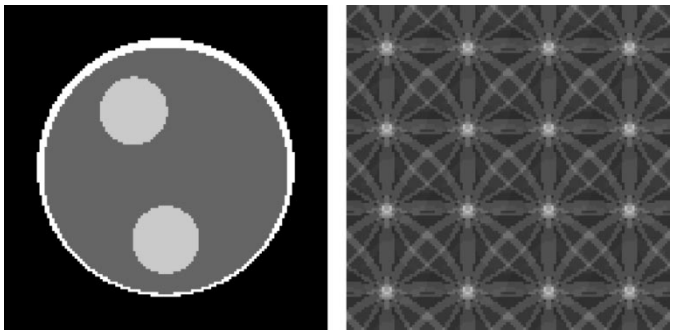

(a) (b)

Fig. 3. (a) Synthetic phantom image; (b) direct Fourier inversion using 1024 uniformly spaced Fourier samples.

C. Estimating Boundaries of Synthetic Phantom

Consider the 128×128 simulated phantom in Fig. 3(a). The phantom consists of four circular boundaries Γ_j, $j = 1, \ldots, 4$ (for the disks D_j, $j = 1, \ldots, 4$), which are parameterized by:

$$\boldsymbol{\zeta}_j(u; \boldsymbol{\theta}_j) = \begin{bmatrix} x_j \\ y_j \end{bmatrix} + r_j \begin{bmatrix} \cos(u) \\ \sin(u) \end{bmatrix}, \qquad j = 1, \ldots, 4. \tag{67}$$

where $\boldsymbol{\theta}_j = [r_j, x_j, y_j]^T$. The true values of the parameters are given by:

$$\begin{aligned} \boldsymbol{\theta}_1 &= \begin{bmatrix} 0.80 \\ 0 \\ 0 \end{bmatrix}, \qquad \boldsymbol{\theta}_2 = \begin{bmatrix} 0.76 \\ 0 \\ -0.02 \end{bmatrix}, \\ \boldsymbol{\theta}_3 &= \begin{bmatrix} 0.21 \\ -0.20 \\ 0.35 \end{bmatrix}, \qquad \boldsymbol{\theta}_4 = \begin{bmatrix} 0.21 \\ 0 \\ -0.45 \end{bmatrix}. \end{aligned} \tag{68}$$

For this problem, $D_3, D_4 \subset D_2 \subset D_1$, and the domain $D = \bigcup_{j=1}^{4} D_j$ is partitioned as follows:

$$D = \bigcup_{k=1}^{4} \Omega_k \tag{69}$$

where

$$\Omega_1 = D_1 \setminus D_2,\ \Omega_2 = D_2 \setminus (D_3 \cup D_4),\ \Omega_3 = D_3,\ \Omega_4 = D_4. \tag{70}$$

The partitioned image $f_1(x, y)$ in the domain D is piecewise constant and given by

$$f_1 = \chi_{\Omega_{11}} + 0.2\chi_{\Omega_{12}} + 0.4\chi_{\Omega_{13}} + 0.4\chi_{\Omega_{14}}, \tag{71}$$

where the intensities for each domain Ω_k

$$f_1 = [1 \quad 0.2 \quad 0.4 \quad 0.4] \tag{72}$$

can be estimated in case *a priori* knowledge of them are not available.

The first imaging example is again image reconstruction from sparse Fourier samples [34]–[37]. Suppose, that 1024 uniformly spaced Fourier samples are taken, which corresponds to $1024/(128 \times 128) = 6.25\%$ of the Nyquist rate. Direct Fourier inversion [Fig. 3(b)] exhibits strong aliasing artifacts. Suppose

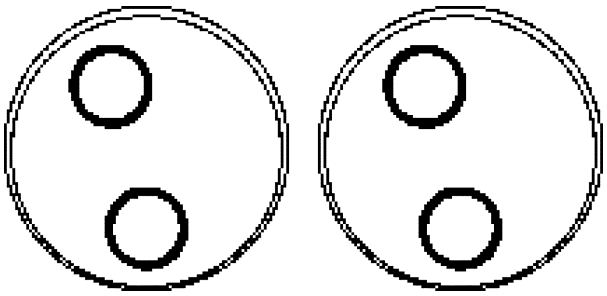

(a) (b)

Fig. 4. Illustration of 95% global confidence regions for parametric estimation of the boundaries of the object in Fig. 3 from 1024 uniformly spaced Fourier samples and samples with additive complex Gaussian noise at SNR = 10 dB assuming (a) known pixel values, and (b) unknown pixel values, respectively.

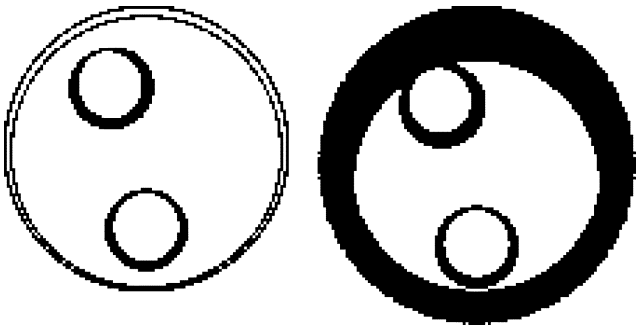

(a) (b)

Fig. 5. Illustration of the 95% global confidence regions for parametric estimation of the boundaries of the object in Fig. 3 from 1024 uniformly spaced Radon samples with sampling parameters of $N_a = N_r = 32$ with additive real Gaussian noise at SNR = 27 dB assuming (a) known pixel values and (b) unknown pixel values, respectively.

we know *a priori* that the image consists of four circles. Then, the imaging problem can be formulated as the estimation of the center locations and the radii of each region, and the CRB for the unknown parameter vectors can be obtained using the techniques described in the previous section. The resulting CRB is a 12×12 matrix and is rather difficult to interpret. We therefore do not show it explicitly.

We have applied the asymptotic global confidence region technique to the example of Fig. 3(a) and computed the 95% asymptotic global confidence region for an example where the Fourier samples are corrupted with additive complex Gaussian noise at SNR = 10 dB. First we assume that intensity (72) is known. Fig. 4(a) illustrates the resulting asymptotic global confidence region, in which asymptotically any unbiased estimate of the boundary will lie with 95% probability. This bound suggests that accurate estimates are possible even under at low sampling rates, if we have *a priori* knowledge of the number of domains and their densities. In addition, Fig. 4(a) tells us that the estimates of small region boundaries are more uncertain while the boundaries of large regions can be estimated very accurately. In Fig. 4(b), we also computed the 95% global confidence regions assuming unknown intensity. Interestingly, the uncertainty contribution from the unknown pixel values are not so significant that we can obtain nearly the same global confidence regions.

The second imaging example is a computed tomography problem. Under the same boundary parameterization (67), if each x-ray always crosses the object boundary twice, then the derivatives of $g_m(\boldsymbol{\theta})$ with respect to $\boldsymbol{\theta}_j = [r_j, x_j, y_j]^T$ are given by

$$\frac{\partial g_m(\boldsymbol{\theta})}{\partial r_j} = \Delta f_j \left(\sum_{l=1}^{2} \frac{1}{\left|\sin\left(s_m - u_{m,j}^l\right)\right|} \right) \tag{73}$$

$$\frac{\partial g_m(\boldsymbol{\theta})}{\partial x_j} = \Delta f_j \left(\sum_{l=1}^{2} \frac{\cos\left(u_{m,j}^l\right)}{\left|\sin\left(s_m - u_{m,j}^l\right)\right|} \right) \tag{74}$$

$$\frac{\partial g_m(\boldsymbol{\theta})}{\partial y_j} = \Delta f_j \left(\sum_{l=1}^{2} \frac{\sin\left(u_{m,j}^l\right)}{\left|\sin\left(s_m - u_{m,j}^l\right)\right|} \right), \tag{75}$$

where $u_{m,j}^l$ is computed by:

$$r_j \cos\left(u_{m,j}^l - s_m\right) = t_m - x_j \cos(s_m) - y_i \sin(s_m). \tag{76}$$

Suppose furthermore that the Radon transform is sampled uniformly both in angle s and in radial direction t with N_a and N_r samples, respectively, such that the total number of samples is $N_r \times N_a = 1024$. We again use the asymptotic global confidence region technique and compute the 95% asymptotic global confidence region for the same synthetic phantom example. Here we assume that the Radon transform samples are corrupted with additive Gaussian noise at SNR = 27 dB.

Fig. 5(a) and (b) illustrate the resulting asymptotic global confidence regions for $N_r = N_a = 32$ assuming both known and unknown intensities, respectively. As observed in Fig. 5(a), the boundary estimates of the large regions are nearly perfect while the boundary estimates of the small regions suffer from some uncertainty. If *a priori* knowledge of intensities of (72) is not available, the uncertainty of the boundary estimates increase as shown in Fig. 5(b). Especially, the uncertainties of the boundaries of the thin ring surrounding the object increase significantly. Note the single wide confidence region in Fig. 5(b) for the two boundaries of the thin ring surrounding the object. This is the union of the individual regions for each of the concentric circles. Compared to Fig. 5(a), we can deduce that the uncertainty of the outer ring estimate is mainly due to the uncertainty of the image value inside the narrow ring. Therefore, the single wide confidence region should be interpreted as uncertainty of the location of the ring as whole rather than suggesting that the outer boundary will be estimated to be interior to the inner boundary of the ring with some probability.

However, if we increase the radial and decrease the angular sampling rates such that $N_r = 64$ and $N_a = 16$, accurate estimation of boundaries can be achieved for both known and unknown intensities as shown Fig. 6(a) and (b). Note that both boundaries of the outermost ring can be nearly perfectly estimated while the other uncertainty regions are significantly reduced compared to those in Fig. 5(a) and (b). Apparently, radial resolution is more important than angular resolution in this example. As observed from this discussion, the CRB and the global confidence region analysis can be used to design the optimal sampling pattern.

The last imaging example is a deconvolution problem with circular Gaussian point spread function given by (6). We again assume that 1024 uniformly spaced samples are taken from

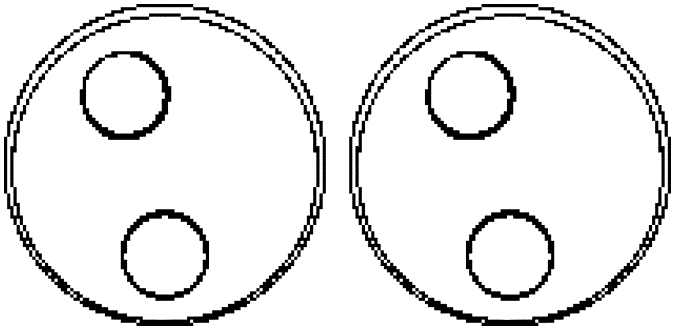

(a) (b)

Fig. 6. Illustration of the 95% global confidence regions for parametric estimation of the boundaries of the object in Fig. 3 from 1024 uniformly spaced Radon samples with sampling parameters of $N_a = 16$ and $N_r = 64$ with additive real Gaussian noise at SNR = 27 dB assuming (a) known pixel values and (b) unknown pixel values, respectively.

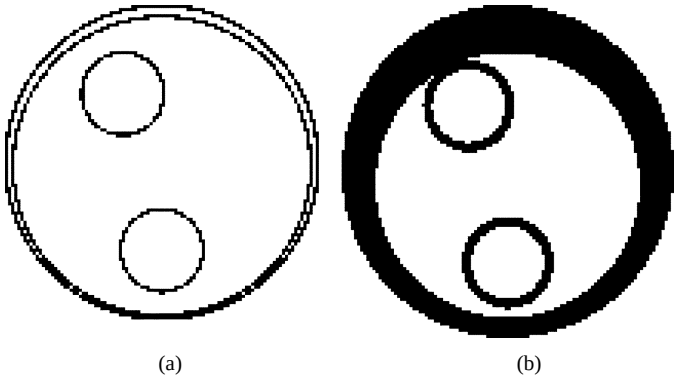

(a) (b)

Fig. 7. Illustration of the 95% global confidence regions for parametric estimation of the boundaries of the object in Fig. 3 from 1024 uniform samples of blurred image with Gaussian point spread function at real Gaussian noise level of SNR = 15 dB and Gaussian point spread function width parameters given by $\nu = 0.2$ assuming (a) known pixel values, and (b) unknown pixel values, respectively.

blurred image. Under the same boundary parameterization (67), the 95% global confidence regions are illustrated in Fig. 7(a) and (b) for both known and unknown intensities, with Gaussian width parameter $\nu = 0.2$. These figures show that *a priori* knowledge of the intensities greatly improves the estimation performance. We also computed the global confidence region for a different value of the width parameter, in Fig. 8(a) and (b). Comparing Figs. 7(a) and 8(a) reveals that, as might be expected, a smaller width parameter ν (less blurring) generally gives better boundary estimation performance. This trend is broken however, for sufficiently small ν (little or no blurring), as shown in Fig. 8(b) as compared to Fig. 7(a), where the uncertainty in the boundary of one of the inner circles is larger for less blurring.

The apparently paradoxical behavior, where "better measurements" appear to lead to "worse estimates" can be explained in the following way. If ν is much smaller than the distance between the sampling points (or their majority) and the object boundaries, then the measurements become essentially decoupled from the boundaries. Small changes in the boundary will only produce vanishing changes in the measurement. This leads to large values of the CRB's on the boundary estimates, and to the wide associated confidence regions. These results provide a bound and asymptotic performance prediction for *unbiased* estimators. Better estimates may be provided by biased estimators (e.g., by bracketing the boundary position between the sampling points), but their performance is not bounded or predicted by the CRB and associated confidence regions.

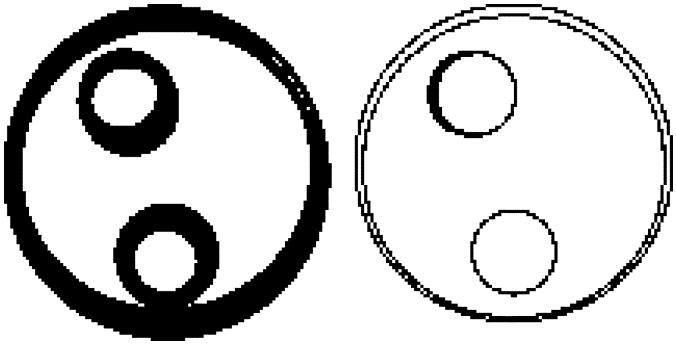

(a) (b)

Fig. 8. Illustration of the 95% global confidence regions for parametric estimation of the boundaries of the object in Fig. 3 from 1024 uniform samples of blurred image with Gaussian point spread function at real Gaussian noise level of SNR = 15 dB assuming known pixel values. Gaussian point spread function width parameters are given by (a) $\nu = 0.4$ and (b) $\nu = 0.00165$, respectively.

VIII. Conclusions

This paper has introduced a general method to compute Cramér–Rao bounds for parametric shape estimation in linear inverse problems, such as computed tomography, Fourier imaging, deconvolution, and etc. Although the imaging map is linear, the dependence of the measurements on the shape of the object, as described by its boundaries, is highly nonlinear. We showed that if object boundaries are parameterized using a finite number of unknown parameters, Cramér–Rao bounds can be obtained using domain derivative techniques. In addition to providing explicit expressions for the components of the Cramér–Rao bounds for computed tomography, Fourier imaging, and deconvolution, our approach can be easily adapted to the particular form of any linear inverse problem with possibly nonlinear observations.

Appendix A
Domain Derivative

The *domain derivative* of the mapping J in (17) is defined in the literature in terms of the infinitesimal variation of J with respect to an infinitesimal deformation of the domain D. We introduce this definition, quote the key result [32], and use it to reformulate the domain derivative in terms of a deformation of the boundary Γ, proving a corollary and Proposition 1.

Suppose the domain $D \subset \mathbb{R}^N$ is deformed by the family of transformations $\mathbf{T}_t$: $\mathbb{R}^N \to \mathbb{R}^N$:

$$\mathbf{T}_t(\mathbf{x}; \mathbf{V}) = \mathbf{x} + t\mathbf{V}(\mathbf{x}), \qquad \mathbf{x} \in \mathbb{R}^N, t \in I = [0, \epsilon), \quad \text{(A.1)}$$

for some $\epsilon > 0$, where N denotes the dimension of the space of our interest (for 2-D images, $N = 2$), and $\mathbf{V}$: $\mathbb{R}^N \to \mathbb{R}^N$ is a

continuously differentiable vector field. The family of deformed domains $\{D_t\}_{t\in I}$ in direction $\mathbf{V}$ is then defined by

$$D_t = \mathbf{T}_t(D;\,\mathbf{V}) \triangleq \left\{\mathbf{z}\in\mathbb{R}^N\colon \mathbf{z}=\mathbf{x}+t\mathbf{V}(\mathbf{x}),\,\mathbf{x}\in D\right\},\qquad t\in I. \tag{A.2}$$

Now we are ready to provide an explicit form of the domain derivative:

Theorem 1 (Sokolowski and Zolesio [32, p. 77]): Suppose the domain D is deformed by the transform $\mathbf{T}_t$ of (A.1), where $\mathbf{V}$ is a continuously differentiable vector field. Suppose, furthermore, that the domain function $J(D)$ is given by

$$J(D)=\int_D Z\,d\mathbf{x}, \tag{A.3}$$

where $d\mathbf{x}$ denotes a differential volume element in $\mathbb{R}^N$. Then, the domain function $J(D)$ is shape differentiable with domain derivative

$$\delta J(D;\,\mathbf{V}) \triangleq \left(\frac{\partial}{\partial t}\int_{D_t} Z\,d\mathbf{x}\right)_{t=0} = \int_D \operatorname{div}(Z\mathbf{V})\,d\mathbf{x}. \tag{A.4}$$

Furthermore, if D is a domain with the boundary $\partial D=\Gamma$ of class C^1, then

$$\delta J(D;\,\mathbf{V}) = \int_\Gamma Z\langle\mathbf{V},\,\mathbf{n}\rangle\,d\Gamma, \tag{A.5}$$

where $\langle\cdot,\,\cdot\rangle$ denotes Euclidean inner product, and $\mathbf{n}\in\mathbb{R}^N$ denotes the outer-normal vector of Γ.

Note that the transformation $\mathbf{T}_t$ of (A.1) is defined on the whole domain $\mathbb{R}^N$. Instead, the deformation of the domain can also be given by the deformation of the boundary:

$$\Gamma_t=\Gamma+t\mathbf{q}=\left\{\mathbf{z}\in\mathbb{R}^N\,\middle|\,\mathbf{z}=\mathbf{x}+t\mathbf{q}(\mathbf{x}),\,\mathbf{x}\in\Gamma\right\}, \tag{A.6}$$

where the vector field $\mathbf{q}\colon\Gamma\to\mathbb{R}^N$ is continuously differentiable. For this transformation, we have the following corollary.

Corollary 1: Let D be a domain with boundary Γ of class C^1. Suppose the boundary Γ is deformed as in (A.6), where $\mathbf{q}$ is a continuously differentiable vector field with respect to arc length. Then, the domain function $J(D)$ of (A.3) is shape differentiable with respect to boundary deformation $\mathbf{q}$, with domain derivative

$$\delta J(D;\,q) \triangleq \left(\frac{\partial}{\partial t}\int_{D_t} Z\,d\mathbf{x}\right)_{t=0} = \int_\Gamma Z\langle\mathbf{q},\,\mathbf{n}\rangle\,d\Gamma, \tag{A.7}$$

where D_t denotes the domain with boundary Γ_t and $\mathbf{n}$ denotes the outer-normal vector of Γ.

Proof: Let $\mathbf{Q}\colon\mathbb{R}^N\to\mathbb{R}^N$ be a continuously differentiable extension of the vector field $\mathbf{q}$ to $\mathbb{R}^N$, and define a new deformation of D by $D_t=\mathbf{T}_t(D)$, where

$$\mathbf{T}_t(\mathbf{x})=\mathbf{x}+t\mathbf{Q}(\mathbf{x}),\qquad \mathbf{x}\in\mathbb{R}^N. \tag{A.8}$$

It follows that $\Gamma_t=\partial D_t$. Using Theorem 1, we have

$$\delta J(D;\,\mathbf{q})=\delta J(D;\,\mathbf{Q})=\int_\Gamma Z\langle\mathbf{Q},\,\mathbf{n}\rangle\,d\Gamma=\int_\Gamma Z\langle\mathbf{q},\,\mathbf{n}\rangle\,d\Gamma, \tag{A.9}$$

where the last equality is because the restriction of $\mathbf{Q}$ to Γ is $\mathbf{q}$ of (A.6). This concludes the proof. □

Next, we use this corollary to prove Proposition 1 (restated here with more detailed conditions).

Proposition 1: Let $D=D(\boldsymbol{\theta})$ be a domain with boundary Γ of class C^1. Suppose the boundary Γ is deformed as

$$\Gamma_t=\Gamma+t\mathbf{b}_i=\{\mathbf{z}|\mathbf{z}=\boldsymbol{\zeta}(u)+t\mathbf{b}_i(u),\,u\in I\}, \tag{A.10}$$

where $\mathbf{b}_i(u)$ is continuously differentiable with respect to $u\in I$. Then, the domain function (17)

$$g(\boldsymbol{\theta})=J[D(\boldsymbol{\theta})]=\int_{D(\boldsymbol{\theta})} Z\,dS \tag{A.11}$$

is shape differentiable with respect to boundary deformation $\mathbf{b}_i$, with domain derivative with respect to parameter θ_i:

$$\frac{\partial g}{\partial\theta_i}=\delta J(D;\,\mathbf{b}_i) = \int_I Z(u)\big(\mathbf{b}_i^T\mathbf{n}\big)(u)\tau(u)\,du,\qquad i=1,\ldots,K, \tag{A.12}$$

where $Z(u)\triangleq Z[\boldsymbol{\zeta}(u)]$, $\tau(u)=\sqrt{\dot{x}(u)^2+\dot{y}(u)^2}$ and $\dot{x}(u)$ and $\dot{y}(u)$ are the derivatives of the components of $\boldsymbol{\zeta}(u)=[x(u),\,y(u)]^T$, and $\mathbf{n}$ denotes the outer-normal vector of Γ.

Proof: Consider the domain deformation (A.10). In order to apply Corollary 1, we set $\mathbf{q}(\boldsymbol{\zeta}(u))=\mathbf{b}_i(u)$, $\boldsymbol{\zeta}(u)\in\Gamma$. Using the regularity conditions for the boundary Γ, we can show that $\mathbf{q}$ is a continuously differentiable vector field with respect to arc length along Γ. This follows, because, by assumption, $\mathbf{b}_i(u)$ is continuously differentiable with respect to $u\in I$, and $\tau(u)=\sqrt{\dot{x}(u)^2+\dot{y}(u)^2}\neq 0$ for all $u\in I$ because of the regularity of Γ.

Now, since $\mathbf{b}_i$ can be represented as a 1-D manifold $\mathbf{b}_i=\{\mathbf{b}_i(u)\colon u\in I\}$, the contour integral (A.7) can be represented as a 1-D integral with respect to the interval I:

$$\delta J(D;\,\mathbf{b}_i)=\int_\Gamma Z\langle\mathbf{q},\,\mathbf{n}\rangle\,d\Gamma = \int_I Z(u)\big(\mathbf{b}^T\mathbf{n}\big)(u)\tau(u)\,du. \tag{A.13}$$

Finally, because the domain deformation (A.10) is with respect to an infinitesimal change in the parameter θ_i, we have

$$\frac{\partial g}{\partial\theta_i}=\delta J(D;\,\mathbf{b}_i),\qquad i=1,\ldots,K. \tag{A.14}$$

This concludes the proof. □

APPENDIX B
PROOF OF LEMMA 1

For any $\epsilon > 0$, define

$$U_\epsilon = \bigcup_i (u_i - \epsilon,\, u_i + \epsilon).$$

Then, because the integrand is identically zero on $I \setminus U_\epsilon$,

$$\int_I \delta(F(u))G(u)\,du = \sum_{i=1}^{L} \int_{u_i-\epsilon}^{u_i+\epsilon} \delta(F(u))G(u)\,du. \quad \text{(A.15)}$$

Next, because the roots are isolated, F continuously differentiable and $F'(u_i) \neq 0$, $\epsilon > 0$ can be chosen such that u_i is the only root of $F(u)$ and $F'(u) \neq 0$ for $u \in (u_i - \epsilon,\, u_i + \epsilon)$, for all i. It follows that $F(u)$ is strictly monotone for $u \in (u_i - \epsilon,\, u_i + \epsilon)$, and has an inverse $H_i(\alpha) = u$, with $\alpha = F(u)$, and $H_i(0) = u_i$. We can therefore use the change of variables $\alpha = F(u)$,

$$\int_{u_i-\epsilon}^{u_i+\epsilon} \delta(F(u))G(u)\,du = \int_{F(u_i-\epsilon)}^{F(u_i+\epsilon)} \delta(\alpha)G(H_i(\alpha))\,\frac{d\alpha}{F'(H_i(\alpha))} \quad \text{(A.16)}$$

where, because of the continuity of F and its monotonicity on the interval $u \in (u_i - \epsilon,\, u_i + \epsilon)$, $F(u_i - \epsilon) < 0$, and $F(u_i + \epsilon) > 0$ if $F'(u_i) > 0$, with opposite signs otherwise. Using the sifting property of $\delta(\cdot)$ we obtain

$$\int_{u_i-\epsilon}^{u_i+\epsilon} \delta(F(u))G(u)\,du = \frac{G(H_i(0))}{|F'(H_i(0))|} = \frac{G(u_i)}{|F'(u_i)|}. \quad \text{(A.17)}$$

Substituting (A.17) into (A.15) concludes the proof.

REFERENCES

[1] C. K. Chui, *Multivariate Splines*. Philadelphia, PA: SIAM, 1988.

[2] C. T. Zahn and R. Z. Roskies, "Fourier descriptors for plane closed curves," *IEEE Trans. Comput.*, vol. C-21, pp. 269–281, Mar. 1972.

[3] E. Persoon and K. S. Fu, "Shape discrimination using Fourier descriptors," *IEEE Trans. Syst., Man, Cybern.*, vol. SMC-7, pp. 170–179, Mar. 1977.

[4] H. L. VanTrees, *Detection, Estimation and Modulation Theory, Part I: Detection, Estimation, and Linear Modulation Theory*. New York: Wiley, 1968.

[5] S. F. Yau and Y. Bresler, "Worst case Cramer–Rao bounds for parametric estimation of superimposed signals with applications," *IEEE Trans. Signal Processing*, vol. 40, pp. 2973–2986, Dec. 1992.

[6] A. J. Devaney and G. A. Tsihirintzis, "Maximum likelihood estimation of object location in diffraction tomography," *IEEE Trans. Signal Processing*, vol. 39, pp. 672–682, Mar. 1991.

[7] G. A. Tsihirintzis and A. J. Devaney, "Maximum likelihood estimation of object location in diffraction tomography, Part II: strongly scattering objects," *IEEE Trans. Signal Processing*, vol. 39, pp. 1466–1470, June 1991.

[8] A. Schatzberg, A. J. Devaney, and A. J. Wittens, "Estimating target location from scattered field data," *Signal Process.*, vol. 40, no. 2–3, pp. 227–237, 1994.

[9] D. J. Rossi and A. S. Willsky, "Reconstruction from projections based on detection and estimation of objects—Part I: Performance analysis," *IEEE Trans. Acoust., Speech, Signal Processing*, vol. ASSP-32, pp. 886–897, Aug. 1984.

[10] P. Stoica and A. Nehorai, "MUSIC, maximum likelihood, and Cramér–Rao bound," *IEEE Trans. Acoust., Speech, Signal Processing*, vol. 37, pp. 720–741, May 1989.

[11] ——, "Performance study of conditional and unconditional direction-of-arrival estimation," *IEEE Trans. Acoust., Speech, Signal Processing*, vol. 38, pp. 1783–1795, Oct. 1990.

[12] A. L. Swindlehurst and P. Stoica, "Maximum likelihood methods in radar array signal processing," *Proc. IEEE*, vol. 86, pp. 421–441, Feb. 1998.

[13] P. S. Naidu and A. Buvaneswari, "A study of Cramér–Rao bounds on object shape parameters from scattered field," *IEEE Trans. Signal Processing*, vol. 47, pp. 1478–1481, May 1999.

[14] D. J. Rossi, A. S. Willsky, and D. M. Spielman, "Object shape estimation from tomographic measurements—A performance analysis," *Signal Process.*, vol. 18, no. 1, pp. 63–87, 1989.

[15] A. O. Hero, R. Piramuthu, J. A. Fessler, and S. R. Titus, "Minimax estimation computed tomography using high resolution anatomical side information and B-spline models," *IEEE Trans. Inform. Theory*, vol. 45, pp. 920–938, Apr. 1999.

[16] J. C. Ye, Y. Bresler, and P. Moulin, "Cramér–Rao bounds for 2-D target shape estimation in nonlinear inverse scattering problems with application to passive radar," *IEEE Trans. Antennas Propagat.*, vol. 49, pp. 771–783, May 2001.

[17] A. Kirsch, "The domain derivative and two applications in inverse scattering," *Inv. Probl.*, no. 9, pp. 81–96, 1993.

[18] J. C. Ye, Y. Bresler, and P. Moulin, "Asymptotic global confidence regions in parametric shape estimation problems," *IEEE Trans. Inform. Theory*, vol. 46, pp. 1881–1895, Aug. 2000.

[19] K. M. Hanson, G. S. Gunningham, and R. J. McKee, "Uncertainty assessment for reconstructions based on deformable geometry," *Int. J. Imag. Syst. Technol.*, vol. 8, pp. 506–512, 1997.

[20] F. Natterer, *The Mathematics of Computerized Tomography*. New York: Teubner, Stuggart, and Wiley, 1986.

[21] S. R. Deans, *The Radon Transform and Some of Its Applications*. New York: Wiley, 1983.

[22] R. E. Blahut, Theory of Remote Image Formation. Cambridge, U.K.: Cambridge Univ. Press, 2001, to be published.

[23] R. N. Bracewell, *Two-Dimensional Imaging*. Englewood Cliffs, NJ: Prentice-Hall, 1995.

[24] D. C. Munson, Jr., J. D. O'Brien, and W. K. Jenkins, "A tomographic formulation of spotlight-mode synthetic aperture radar," *Proc. IEEE*, vol. 71, pp. 917–925, Aug. 1983.

[25] M. Soumekh, *Fourier Array Imaging*. Englewood Cliffs, NJ: Prentice-Hall, 1994.

[26] Z. P. Liang and P. C. Lanterbur, *Principle of Magnetic Resonance Imaging: A Signal Processing Perspective*. New York: IEEE Press, 2000.

[27] D. Colton and A. Kirsch, *Inverse Acoustic and Electromagnetic Scattering*. Berlin, Germany: Springer Verlag, 1992.

[28] G. C. H. Chuang and C. C. Jay Kuo, "Wavelet descriptor of planar curves: Theory and applications," *IEEE Trans. Image Processing*, vol. 5, pp. 56–70, Jan. 1996.

[29] P. Wunsch and A. F. Laine, "Wavelet descriptors for multiresolution recognition of handprinted characters," *Pattern Recognit.*, vol. 28, no. 8, pp. 1237–1249, 1995.

[30] J. Rissanen, "Modeling by shortest data description," *Automatica*, vol. 14, pp. 465–471, 1978.

[31] N. Schmid, Y. Bresler, and P. Moulin, "Complexity regularized shape estimation from noisy Fourier data," in *Proc. 9th IEEE Int. Conf. Image Processing (ICIP'02)*, Rochester, NY, Sept. 2002.

[32] J. Sokolowski and J. Zolesio, *Introduction to Shape Optimization: Shape Sensitivity Analysis*. New York: Springer-Verlag, 1991.

[33] J. Munkres, *Analysis on Manifolds*. Englewood Cliffs, NJ: Prentice-Hall, 1991.

[34] R. Venkataramani and Y. Bresler, "Perfect reconstruction formulas and bounds on aliasing error in sub-Nyquist nonuniform sampling of multiband signals," *IEEE Trans. Inform. Theory*, vol. 46, pp. 2173–2183, Sept. 2000.

[35] Y. Bresler and P. Feng, "Spectrum-blind minimum-rate sampling and reconstruction of 2-D multiband signals," in *Proc. 3rd IEEE Int. Conf. Image Processing (ICIP'96)*, vol. I, Lausanne, Switzerland, Sept. 1996, pp. 701–704.

[36] R. Venkataramani and Y. Bresler, "Further results on spectrum blind sampling of 2D signals," in *Proc. IEEE Int. Conf. Image Proc.*, vol. 2, Chicago, Oct. 1998, pp. 752–756.

[37] Y. Bresler, M. Gastpar, and R. Venkataramani, "Image compression on-the-fly by universal sampling in Fourier imaging systems," in *Proc. 1999 IEEE Information Theory Workshop on Detection, Estimation, Classification, and Imaging*, Santa-Fe, NM, Feb. 1999, p. 48.

[38] Metastatic bronchogenic carcinoma. [Online]. Available: http://www.med.harvard.edu/AANLIB/home.htm.

Jong Chul Ye (M'02) received the Ph.D. degree in electrical and computer engineering from the School of Electrical and Computer Engineering, Purdue University, West Lafayette, IN, and the M.Sc. and B.Sc. degree in electrical engineering with honors from the Control and Instrumentation Engineering Department of Seoul National University, Korea.

He is currently with Wireless Communication and Networking Department of Philips Research, Briarcliff Manor, NY. Prior to joining Philips, he worked at the Coordinated Science Laboratory of University of Illinois at Urbana-Champaign as a Postdoctoral Research Associate, and also briefly worked at the Image Science Laboratory of Polaroid Corporation. His current research interests include statistical signal processing and their applications to inverse problems, video compression and streaming for wireless in-home networking, and digital imaging for printing and camera applications.

Dr. Ye received Korean Government Overseas Scholarship Award (1995–1998) for his graduate study.

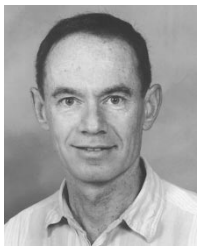

Yoram Bresler (F'99) received the B.Sc. (cum laude) and M.Sc. degrees from the Technion, Israel Institute of Technology, in 1974 and 1981 respectively, and the Ph.D. degree from Stanford University, Stanford, CA, in 1986, all in electrical engineering.

From 1974 to 1979, he served as an Electronics Engineer in the Israeli Defense Force. From 1985 to 1987, he was a Research Associate at the Information Systems Laboratory at Stanford University, working on sensor array processing and medical imaging. In 1987, he joined the University of Illinois at Urbana-Champaign, where he is currently a Professor in the Department of Electrical and Computer Engineering and the Bioengineering Program, and Research Professor at the Coordinated Science Laboratory. In 1995–1996 he spent a sabbatical leave at the Technion, Israel Institute of Technology. His current research interests include multidimensional and statistical signal processing and their applications to inverse problems in imaging. He is on the editorial board of *Machine Vision and Applications*.

Dr. Bresler was an Associate Editor for the IEEE TRANSACTIONS FOR IMAGE PROCESSING in 1992–1993 and a Member of the IEEE Image and Multidimensional Signal Processing Technical Committee in 1994–1998. In 1988 and 1989, he received the Senior Paper Awards from the IEEE Signal Processing Society, and a paper he coauthored with one of his students received the Young Author Award from the same society in 2002. He is the recipient of a 1991 NSF Presidential Young Investigator Award, the Technion, Israel Institute of Technology Fellowship in 1995, and the Xerox Senior Award for Faculty Research in 1998. He was named a University of Illinois Scholar in 1999, and appointed as an Associate at the Center for Advanced Study of the University in 2001–2002.

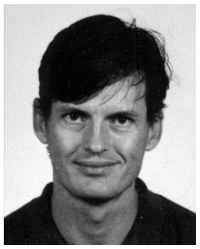

Pierre Moulin (M'90–SM'98–F'02) received the degree of Ingénieur civil électricien from the Faculté Polytechnique de Mons, Belgium, in 1984, and the M.Sc. and D.Sc. degrees in electrical engineering from Washington University in St. Louis in 1986 and 1990, respectively.

He was a Researcher at the Faculté Polytechnique de Mons in 1984–1985 and at the Ecole Royale Militaire in Brussels, Belgium, in 1986–1987. He was a Research Scientist at Bell Communications Research, Morristown, NJ, from 1990 to 1995. In 1996, he joined the University of Illinois at Urbana-Champaign, where he is currently an Associate Professor in the Department of Electrical and Computer Engineering and a Research Associate Professor in the Beckman Institute and in the Coordinated Science Laboratory. His fields of professional interest are image and video processing, compression, statistical signal processing and modeling, nonparametric function estimation, information theory, information hiding, and the application of multiresolution signal analysis, optimization theory, and fast algorithms to these areas.

Dr. Moulin has served as an Associate Editor of the IEEE TRANSACTIONS ON INFORMATION THEORY and the IEEE TRANSACTIONS ON IMAGE PROCESSING, Co-chair of the 1999 IEEE Information Theory Workshop on Detection, Estimation, Classification and Imaging, Chair of the 2002 NSF Workshop on Signal Authentication, and Guest Associate Editor of the IEEE TRANSACTIONS ON INFORMATION THEORY's 2000 special issue on information-theoretic imaging. Currently he is Area Editor of the IEEE TRANSACTIONS ON IMAGE PROCESSING, Guest Associate Editor of the IEEE TRANSACTIONS ON SIGNAL PROCESSING's 2003 special issue on data hiding, and a member of the IEEE IMDSP Technical Committee. He received a 1997 Career award from the National Science Foundation and the IEEE Signal Processing Society 1997 Senior Best Paper award. He is also the co-author (with J. Liu) of a paper that received an IEEE Signal Processing Society 2002 Young Author Best Paper Award.